J Solid State Electrochem (2012) 16:1965–1973
DOI 10.1007/s10008-011-1586-2

ORIGINAL PAPER

Photoelectrochemical properties of tungsten trioxide thin film electrodes prepared from facet-controlled rectangular platelets

Fumiaki Amano · Min Tian · Bunsho Ohtani · Aicheng Chen

Received: 22 August 2011 / Revised: 29 October 2011 / Accepted: 31 October 2011 / Published online: 2 December 2011

Abstract The control of anisotropic crystal growth is critical for directing the orientation of crystal lattice planes, and it plays a key role towards understanding the effects of different planes on chemical reactions. Here, we report on the photoelectrochemical properties of plate-structured tungsten trioxide (WO_3) thin films prepared from facet-controlled rectangular platelets of hydrotungstite ($WO_3{\cdot}2H_2O$) and tungstite ($WO_3{\cdot}H_2O$), which are directly grown on tungsten substrates. The WO_3 thin films, prepared via $WO_3{\cdot}2H_2O$ platelets, show relatively stable current for photoelectrochemical water splitting and methanol oxidation. On the other hand, the photocurrent of the WO_3 thin films prepared via $WO_3{\cdot}H_2O$ platelets was significantly decreased during the photoelectrochemical oxidation of water, which is likely due to the accumulation of partially oxidized intermediates such as peroxo species on the surface. These results indicate that the surface nanostructures of WO_3 may have a significant influence on photoelectrode efficiency and selectivity for the catalytic oxygen evolution reaction.

Keywords Crystal growth · Layered compounds · Nanostructures · Photoenergy conversion · Thin films

Introduction

The design and preparation of anisotropic nanostructures are important issues to address toward the improvement of their inherent kinetics and, hence, the development of novel functional materials. Many researchers have been intrigued by two-dimensional crystalline nanostructures due to their potential in diverse applications encompassing catalysts, photocatalysts, sensors, electrodes, and device building blocks, to name a few [1–6]. Nanosheets may be obtained by the exfoliation of layered crystalline compounds using the intercalation of organic molecules since these layered materials are comprised of stacks of crystalline nanosheets. Nanoplates have frequently been prepared by crystal growth in the liquid phase, with or without structure-directing agents, which prohibit crystal growth in certain directions [7–12]. Under close-to-equilibrium conditions, crystal lattice planes that possess high free energy surfaces are eliminated during growth. The facets that possess lower energy are exposed on polyhedral single crystals in order to minimize the total energy of the particle [13, 14]. Therefore, the equilibrium shape may be determined via the Wulff construction, which is based on the surface energies that are dependent on the structure of the crystal lattice planes [15].

Recently, much attention has been focused on rectangular platelets of tungstite ($WO_3{\cdot}H_2O$) or hydrotungstite ($WO_3{\cdot}2H_2O$) since they may be transformed to an

Electronic supplementary material The online version of this article (doi:10.1007/s10008-011-1586-2) contains supplementary material, which is available to authorized users.

F. Amano · B. Ohtani
Catalysis Research Center, Hokkaido University, Sapporo 001-0021, Japan

M. Tian · A. Chen
Department of Chemistry, Lakehead University, Thunder Bay, Ontario P7B 5E1, Canada

Present Address:
F. Amano (✉)
Department of Chemical and Environmental Engineering, University of Kitakyushu, Kitakyushu 808-0135, Japan
e-mail: amano@kitakyu-u.ac.jp

important semiconductor material, i.e., tungsten(VI) oxide (WO_3), without a significant change in their plate-like morphology [16–20]. WO_3 has been studied extensively as a visible-light-responsive photocatalyst and photoelectrode [21–28]. The fabrication of structure-controlled WO_3 thin films has been one of the research target areas undertaken in an effort to improve the photoelectrochemical properties of anodic reactions [18, 19, 29–34]. $WO_3{\cdot}H_2O$ (orthorhombic, a=0.525 nm, b=1.071 nm, c=0.513 nm) exhibits a layered crystal structure comprised of stacked corner-sharing $WO_5(OH_2)$ octahedral sheets via hydrogen bonding (Fig. S1a in "Electronic supplementary material") [35]. The tungsten atom embedded within the $WO_5(OH_2)$ octahedron is coordinated by five oxygen atoms and a water molecule. For $WO_3{\cdot}2H_2O$ (monoclinic, a=1.057 nm, b=1.380 nm, c=1.057 nm, β=91.04°), a second water molecule is placed within the interlayer as a structural water molecule (Fig. S1b in "Electronic supplementary material") [36]. Sugahara et al. have reported that $WO_3{\cdot}H_2O$ platelets prepared from an inorganic–organic compound exhibited a large area of {101} facets along the tungsten oxide sheets, which was converted to single-crystal monoclinic WO_3 platelet with the preferential orientation of {001} planes in relation to the basal plane [16]. Since reactivity is thought to be contingent on surface free energy, controlling the area of reactive facets within anisotropic nanostructures is critical for the improvement of properties that are conducive for chemical reactions. However, there are few insights available as relates to the effect of the specific crystal lattice planes on photoelectrochemical properties. We therefore attempted to fabricate thin film electrodes that were comprised of WO_3 platelets with a large facet area. Rectangular crystalline platelets of $WO_3{\cdot}H_2O$ and $WO_3{\cdot}2H_2O$ were grown directly on a tungsten substrate by a facile hydrothermal reaction method. The platelets were subsequently converted to crystalline WO_3 platelets via calcination. Each WO_3 platelet was expected to exhibit similar crystal lattice planes; however, their photoelectrochemical properties were found to be different.

Experimental section

Preparation

The hydrothermal reaction was performed using a Teflon-lined autoclave. Tungsten sheets (99.95% purity, 0.25 mm in thickness) were heated in 8 mL of a 1.5 mol L^{-1} nitric acid at 100 °C for 3 h, 140 °C for 2 h, or 180 °C for 1 h, respectively. The films thus obtained were rinsed with pure water and dried at room temperature (ca. 20 °C). Prior to calcination, the samples were denoted as Wx-y h, in which x and y indicate the hydrothermal reaction temperature in the unit of °C and the reaction time in the unit of hours, respectively. The samples that were calcined at 450 °C for 3 h were denoted as Wx-y h-C.

Characterization

SEM images were obtained using a JEOL JSM-7400 F field emission SEM. Micro-Raman spectroscopy was performed using a Jobin Yvon T64000 system with a 514-nm laser. TEM images and electron diffraction patterns were recorded on a JEOL JEM-2100 F field emission TEM. Samples were deposited on a TEM grid using ethanol and were evacuated and dried at room temperature.

Photoelectrochemical measurement

Photoelectrode reactions were carried out in a glass cell utilizing a three-electrode configuration, which included a platinum coil as a counter electrode and a silver/silver chloride (Ag/AgCl) electrode in an aqueous solution of 1 mol L^{-1} potassium chloride (+0.222 V vs a standard hydrogen electrode) as a reference electrode. The thin films prepared in this study were welded to a titanium wire and used as the working electrode. A 50-W metal halide lamp (ADAC Systems Cure Spot 50 lamp) was used for photo-irradiation. The primary distribution of light was ultraviolet A (UV-A) and blue-visible light (300–450 nm). The light was introduced into the cell using a fiber optic cable, which was placed above the electrode. The distance between the fiber optic tip and the electrode surface was adjusted to 15 mm. Voltammetric and impedance experiments were performed using a computer-controlled potentiostat (Radiometer analytical VolataLab 40). For linear sweep and cyclic voltammetry, the applied potential was swept from zero to the anodic direction by a scanning rate of 50 mV s^{-1}. For potentiostatic measurement, the potential was adjusted to +0.8 $V_{Ag/AgCl}$. Dilute sulfuric acid (0.1 mol L^{-1} H_2SO_4, 20 mL) was used as the electrolyte solution, which was stirred continuously via a small magnetic bar. In the case of the photoelectrochemical oxidation of methanol, the concentration of methanol was adjusted to 10 vol.%. Capacitance measurements for the Mott–Schottky plot were performed in the dark at a frequency of 1 kHz with applied sinusoidal amplitude of 10 mV. The capacitance of the space charge layer (C) was calculated from the imaginary part of the impedance, assuming a series capacitor–resistor model. The E_{fb} and N_D were obtained from a plot of C^{-2} vs applied potential (E) via Mott–Schottky equation:

$$1/C^2 = (2/q\varepsilon\varepsilon_0 N_D)(E - E_{fb} - kt/q) \quad (1)$$

where q is elementary electric charge, ε is dielectric constant (taken as 50 for WO_3 [37]), ε_0 is permittivity of vacuum, k is Boltzmann's constant, and t is temperature.

Results and discussion

Morphology and crystalline phase

A method previously reported by Widenkvist et al. was modified and utilized in the preparation of thin films with plate-like structures of $WO_3 \cdot H_2O$ and $WO_3 \cdot 2H_2O$ [17]. The hydrothermal reaction of tungsten sheets in dilute nitric acid resulted in the production of yellowish-green thin films on their surfaces. The morphology of the obtained thin films was examined using a scanning electron microscope (SEM). The insets in Fig. 1 depict the top-view SEM images of W100-3 h, W140-2 h, and W180-1 h, which were hydrothermally prepared at 100 °C for 3 h, 140 °C for 2 h, and 180 °C for 1 h, respectively. Rectangular plate-like shapes having dimensions of a few micrometers were observed on the surface of the thin films. The average lengths of the platelets were 540, 2,100, and 1,500 nm for W100-3 h, W140-2 h, and W180-1 h, respectively. The average thicknesses of the platelets were 66, 220, and 210 nm for W100-3 h, W140-2 h, and W180-1 h, respectively [38]. A similar morphology has been reported for a $WO_3 \cdot H_2O$ thin film, formed when a tungsten substrate was immersed in nitric acid at 50 °C and then annealed at 100 °C [17]. The SEM images of the thin films following calcination at 450 °C (W100-3 h-C, W140-2 h-C, and W180-1 h-C) are also shown in Fig. 1. No morphological changes were observed as a result of calcination.

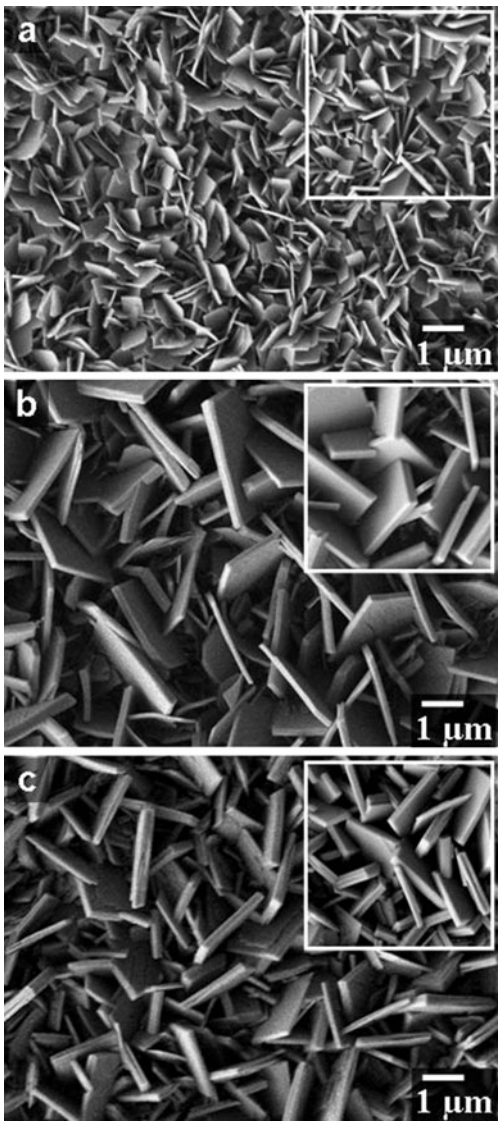

Fig. 1 SEM images of the calcined thin films: **a** W100-3 h-C, **b** W140-2 h-C, and **c** W180-1 h-C. *Insets* show SEM images of the thin films before calcination

Micro-Raman spectroscopy was performed to evaluate the crystalline composition of the thin films. Figure 2 shows Raman spectra of the thin films prior to calcination. W100-3 h exhibited characteristic bands that correspond to $WO_3 \cdot 2H_2O$, with two narrow bands at 661 and 681 cm^{-1}, assignable to the stretching mode of the W–O–W bonds, and a sharp band at 960 cm^{-1}, assignable to the stretching mode of terminal W=O bonds [39]. W180-1 h exhibited only a broad band centered at 644 cm^{-1}, assignable to the stretching mode of W–O–W bonds, and an intense band at 948 cm^{-1}, assignable to the stretching mode of terminal W=O bonds, which are consistent with the spectra of $WO_3 \cdot H_2O$ [39]. Raman spectrum of W140-2 h clearly indicates that the thin film exhibited two crystalline components: $WO_3 \cdot 2H_2O$ and $WO_3 \cdot H_2O$. Figure 3 shows Raman spectra of the thin films following calcination. The W=O vibration of ~950 cm^{-1} disappeared, subsequent to calcination for each film [30, 39]. The characteristic bands (272, 327, 716, and 808 cm^{-1}) were assignable to monoclinic WO_3 rather than hexagonal and orthorhombic WO_3 [40]. The bands at 716 and 808 cm^{-1} and the

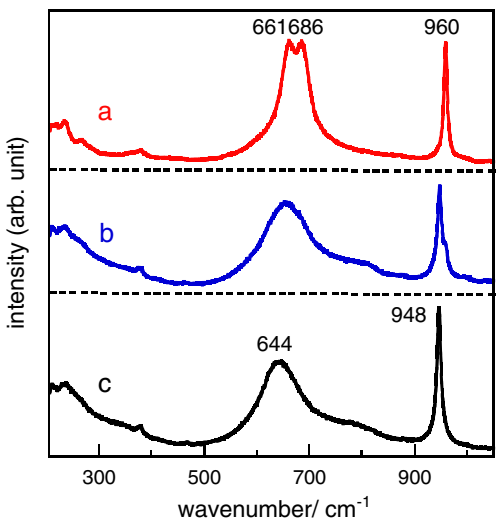

Fig. 2 Raman spectra of the thin films before calcination: **a** W100-3 h, **b** W140-2 h, and **c** W180-1 h

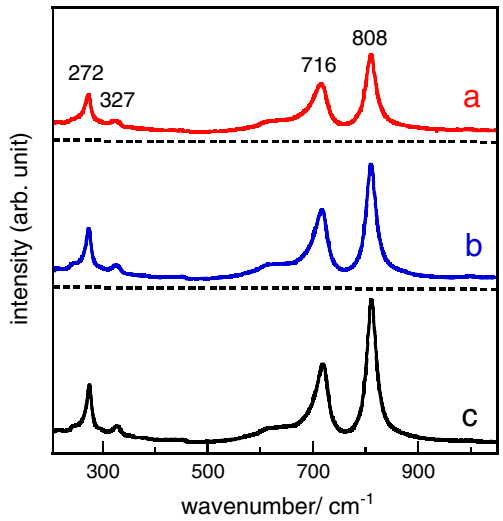

Fig. 3 Raman spectra of the calcined thin films: **a** W100-3 h-C, **b** W140-2 h-C, and **c** W180-1 h-C

bands at 272 and 327 cm^{-1} are attributable to the stretching and bending modes of W–O–W bonds [40]. The shoulder that appeared at ~610 cm^{-1} is also attributable to the stretching mode.

Crystalline orientation of platelets

The crystal orientation of the platelets that were dislodged from the thin films was characterized using a transmission electron microscope (TEM). Figure 4a shows the TEM images and selected area electron diffraction (SAED) patterns of $WO_3 \cdot 2H_2O$ platelets derived from W100-3 h. The ordered spots within the SAED pattern indicate that the platelets possess the nature of a single crystal. The lattice spacing of 0.38, 0.26, and 0.37 nm was consistent with the interplanar distances of {20–2}, {400}, and {202} of monoclinic $WO_3 \cdot 2H_2O$, respectively. The angles between the {400} reflections and the {20–2} and {202} reflections were close to the calculated values (45.3° and 44.2°). Therefore, the pattern would be indexed to $WO_3 \cdot 2H_2O$ with the [010] zone axis. The direction of [20–2] and [202] were parallel to the side edge of the platelet. These results indicate that the $WO_3 \cdot 2H_2O$ platelets exhibit a large rectangular surface of the {010} facet and sides of {10–1} and {101} facets. Figure 4b, c show TEM images and the SAED pattern of $WO_3 \cdot H_2O$ platelets derived from W140-2 h and W180-1 h. These patterns might be indexed to orthorhombic $WO_3 \cdot H_2O$ with the [010] zone axis since the lattice spacings of 0.26 and 0.37 nm were consistent with the interplanar distances of {002} and {101}, and their angles were close to the calculated value of 44.4°. The direction of [101] and [10–1] were parallel to the edges of the platelet, indicating that the $WO_3 \cdot H_2O$ platelets exhibit a large rectangular surface comprised of {010} facets and sides comprised of {101} facets.

Figure 5 presents TEM images and SAED patterns of WO_3 platelets dislodged from the thin films after calcination. The TEM images show that the surfaces of the platelets are not flat. A number of segments of the platelets exhibited ordered SAED patterns, indicating a single crystalline nature. However, other segments were comprised of several crystallites. The transformation of $WO_3 \cdot 2H_2O$ to $WO_3 \cdot H_2O$ occurs under mild conditions such as 120 °C [41], and crystal transformation to monoclinic WO_3 is considered to proceed through the dehydration of hydroxyl groups within crystalline $WO_3 \cdot H_2O$. The plate-like structures were retained during crystal transformation. However, the transformation generates strains in the crystalline platelets. Therefore, only a portion of the platelet may be transformed to the single-crystal WO_3 species. The patterns in Fig. 5 might be indexed to monoclinic WO_3 with the [100] zone axis. This suggests that the {100} planes are parallel to the basal plane of platelet. This crystalline orientation is not consistent with the results reported by Sugahara et al. who reported that single-crystalline monoclinic WO_3 nanoplates exhibited a preferential orientation of {001} planes parallel to the basal plane [16]. Since the platelets observed in this study are not perfect single crystals and do not possess uniformly flat surface structures, we cannot define the distinct crystalline facet that is preferentially exposed on the surface.

Photoelectrochemical properties

The photoelectrochemical performance of the calcined thin films for water splitting in a dilute sulfuric acid depended significantly on both temperature and the duration of the hydrothermal reaction [38]. The thin films that were prepared at optimized reaction times (1, 2, and 3 h at 180, 140, and 100 °C, respectively) exhibited high anodic photocurrents that were measured by linear sweep voltammograms in 0.1 mol L^{-1} H_2SO_4 (Fig. S2 in "Electronic supplementary material"). In the dark, the films exhibited an anodic current at~+0.1 $V_{Ag/AgCl}$. The dark current is attributable to the electrochemical oxidation of partially reduced WO_3. There was difference in the current–potential curves in the dark and under photoirradiation. The anodic currents observed only under photoirradiation could be assignable to the oxidation of water by photogenerated holes in the WO_3 thin film platelets. The dark current was not influenced by adding methanol (Fig. S3 in "Electronic supplementary material"). On the other hand, the photocurrent was enhanced in the presence of methanol, which served as a strong electron donor, since the reaction between photogenerated holes with methanol is more rapid than that with water [42, 43]. In addition, hydroxy methyl

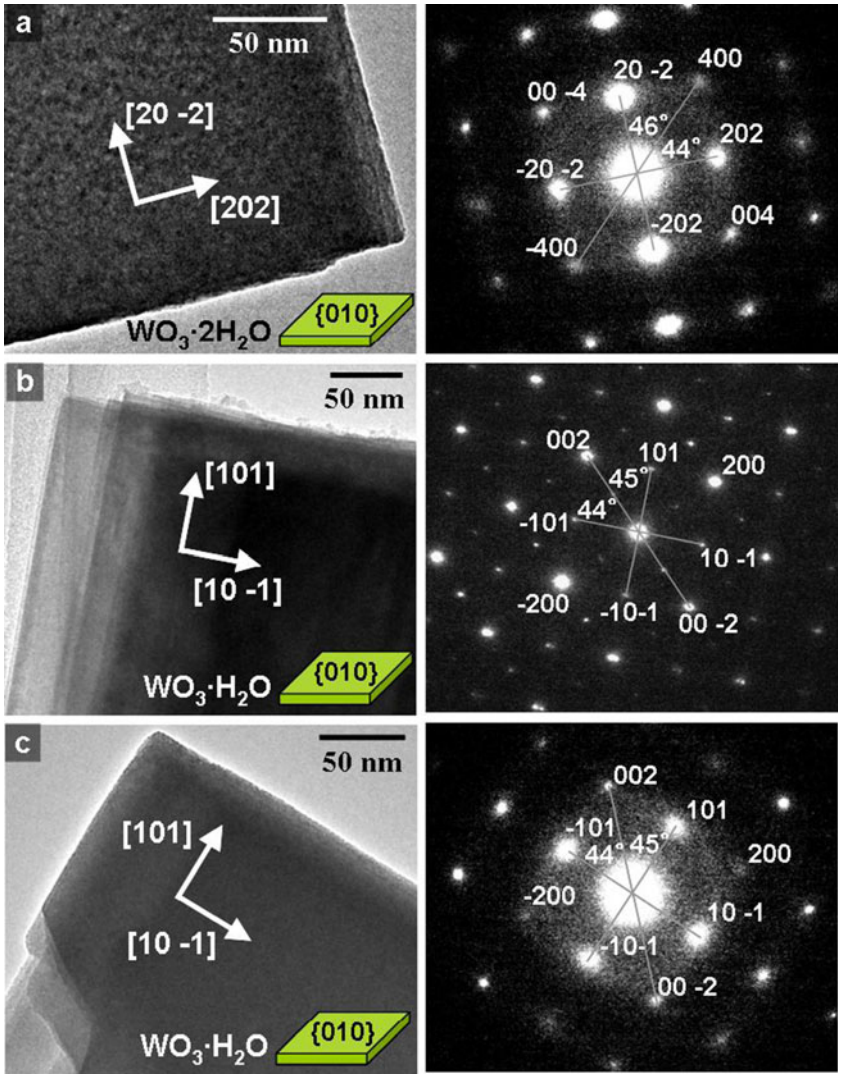

Fig. 4 TEM images and SAED patterns of $WO_3 \cdot H_2O$ and $WO_3 \cdot 2H_2O$ platelets dislodged from the thin films: **a** W100-3 h, **b** W140-2 h, and **c** W180-1 h

radicals ($\cdot CH_2OH$), which are generated by the single electron oxidation of methanol, may inject another electron into the conduction band of WO_3 owing to large negative redox potentials [44, 45]. The onset potentials for anodic current due to photoelectrochemical oxidation of methanol were located at ca. +0.1 V vs Ag/AgCl ($V_{Ag/AgCl}$), which corresponds to a potential of +0.38 V versus a reversible hydrogen electrode (RHE; $V_{RHE}=V_{Ag/AgCl}+0.222+0.059$ pH). These potentials were consistent with the flat-band potentials of the thin films, +0.06−+0.10 $V_{Ag/AgCl}$ (Table S1 in "Electronic supplementary material"), which were estimated from Mott–Schottky plots that were obtained in the dark (Fig. S4 in "Electronic supplementary material"). These results indicate that anodic polarization in the space charge layer is essential for the induction of the photoreaction.

Figure 6a, b shows current–time plots for the photoelectrochemical oxidation of water and methanol at +0.8 $V_{Ag/AgCl}$ (+1.08 V_{RHE}), which is more negative than the potential for water oxidation (+1.23 V_{RHE}). It should be noted that water oxidation is induced by assistance of photoenergy. Similarly to the results of linear sweep voltammetry, the photocurrents for methanol oxidation were higher than that for water oxidation. The photocurrents gradually decreased over the course of the irradiation time. However, the decrease observed for water splitting was larger than that for methanol oxidation. Figure 6c presents the time course increments of photocurrent following the addition of methanol, which is the ratio of photocurrent for methanol oxidation to that for water splitting. At the initial stage of the reactions, the increment values were close to two. Such phenomena are known as "current doubling" effect [44, 45]. If the efficiencies of the holes that react with water and methanol are identical and the efficiency of a single electron transfer from $\cdot CH_2OH$ to the conduction band of WO_3 is 100%, the current derived from methanol oxidation should be two times higher than that which is due to water splitting. Therefore, the value

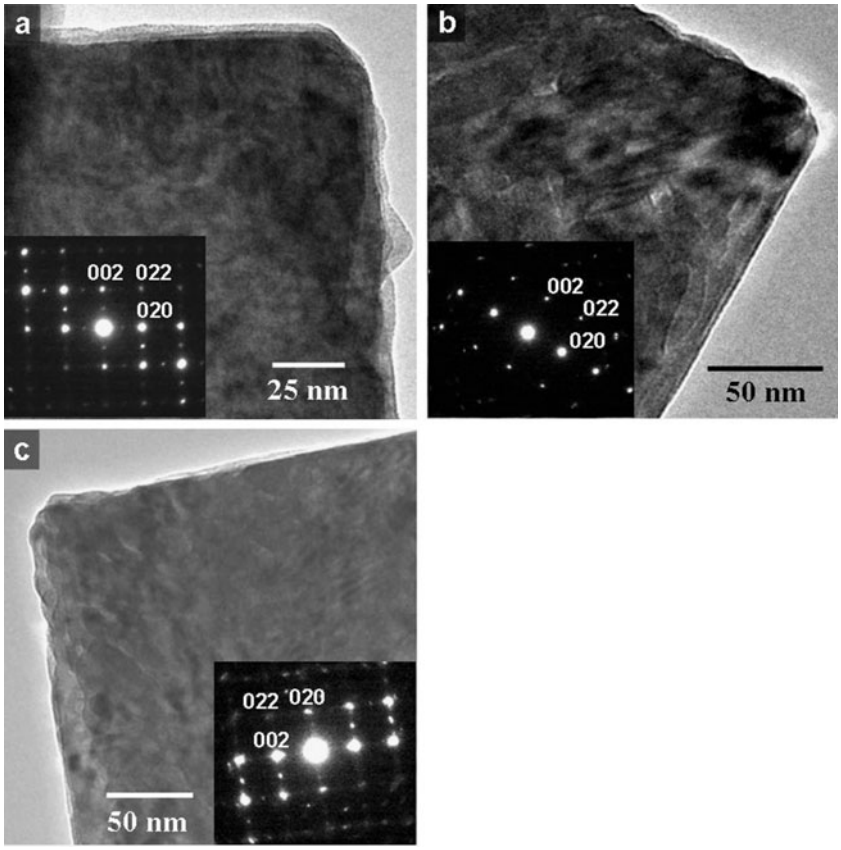

Fig. 5 TEM images and SAED patterns of WO_3 platelets dislodged from the calcined thin films: **a** W100-3 h-C, **b** W140-2 h-C, and **c** W180-1 h-C

near two might simply be assignable to the current doubling effect. The increment value of W100-3 h-C was ca. 2 and almost constant during the photoelectrochemical reactions, suggesting that the surface reaction rates for both reactants were the same, although methanol oxidation to produce $\cdot CH_2OH$ is a single-electron reaction, whereas water oxidation to produce oxygen is a four-electron reaction. On the other hand, the values of W140-2 h-C and W180-1 h-C were increased through the course of the reaction. Since it seems that the photocurrent for methanol oxidation is relatively stable, the increments during the reaction could be related to the significant decrease in the photocurrent during the photoelectrochemical oxidation of water. In fact, the photocurrent of W180-1 h-C decreased to one third after the reaction proceeded for 4 h. The photocurrent of W100-3 h-C was more stable during water oxidation than that of W140-2 h-C and W180-1 h-C, although the photocurrent for methanol oxidation was lower than that of W140-2 h-C and W180-1 h-C. It was found that preparation at higher temperatures resulted in the production of thin films with a rate that declines more rapidly during photoelectrochemical water oxidation. The crystal orientations of the platelets utilized as precursors for the fabrication of WO_3 thin films were almost identical (e.g., the single crystalline platelets exhibited {010} planes of $WO_3 \cdot H_2O$ or $WO_3 \cdot 2H_2O$), and the same conditions were applied for calcination. Therefore, the surface structures of the WO_3 platelets are expected to be similar. However, the photoelectrochemical properties of the WO_3 thin films prepared via the $WO_3 \cdot H_2O$ platelets were distinct from the WO_3 thin films prepared via the $WO_3 \cdot 2H_2O$ platelets.

Regeneration of photoelectrode performance

Figure 7 shows cyclic voltammograms of W180-1 h-C before and after the photoelectrochemical oxidation of water for 4 h. The dark anodic current observed at ~+0.1 $V_{Ag/AgCl}$ disappeared when scanning from right to left since WO_3 is fully oxidized at positive potentials. The photocurrent at potentials more positive than +0.6 $V_{Ag/AgCl}$ was decreased after the photoelectrochemical reaction, but it was increased by the repetition of cyclic voltammetry and restored to the photocurrent similar to that of the original W180-1 h-C after 7 cycles. The regeneration of photocurrent indicates that there was no physical damage within the electrode. Oxygen evolution by water oxidation is a four-electron reaction which is kinetically slower than methanol oxidation [42, 43]. Partially oxidized byproducts such as hydrogen peroxide, the production of which is a two-electron reaction, are supposed to be generated on the surface as an intermediate and act to retard the surface reaction rate [46, 47]. WO_3 photoanodes have been

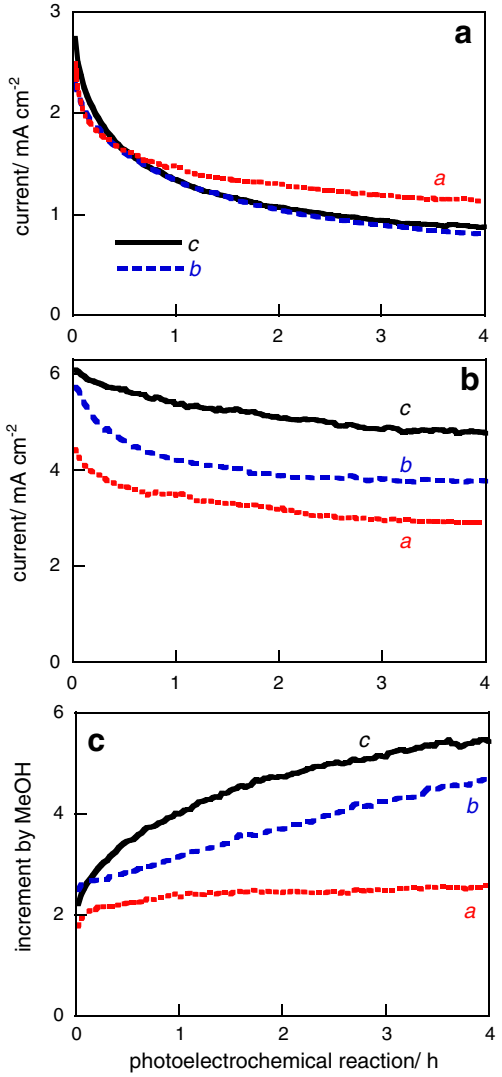

Fig. 6 Photoelectrochemical oxidation of **a** water in 0.1 mol L^{-1} H_2SO_4 at +0.8 $V_{Ag/AgCl}$ and **b** methanol in 0.1 mol L^{-1} H_2SO_4 with 10 vol.% methanol at +0.8 $V_{Ag/AgCl}$: (*a*) W100-3 h-C, (*b*) W140-2 h-C, and (*c*) W180-1 h-C. **c** Increment of photocurrent by methanol addition

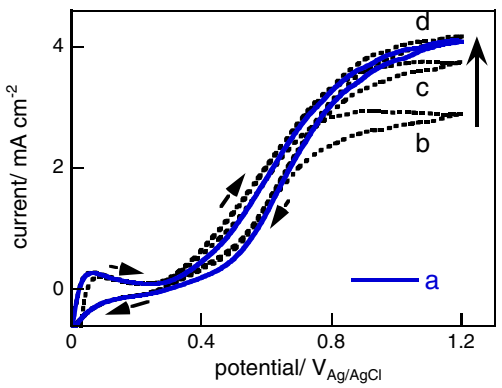

Fig. 7 Cyclic voltammograms under photoirradiation of (*solid curve*, *a*) original W180-1 h-C and (*dashed curves*, *b–d*) W180-1 h-C after 4 h of photoelectrochemical reaction; (b) 1st cycle, (c) 5th cycle, and (d) 7th cycle

reported to produce peroxo species as well as oxygen during the photooxidation of water, although oxygen production is thermodynamically more feasible than the formation of hydrogen peroxide [46, 47]. The accumulation of peroxo species on the surface is considered to cause the gradual loss of photoactivity. A negative potential in the cyclic voltammetry might be effective for the reduction and removal of partially oxidized species, which results in the regeneration of the photoelectrode performance. Based on the above consideration, the decrease of photocurrent during photoelectrochemical oxidation of water is attributable to the formation of partially oxidized products on the surface, such as peroxo species.

Figure 8 shows the electrochemical impedance spectroscopy (EIS) response of W180-1 h-C during the photoelectrochemical oxidation of water at +0.8 $V_{Ag/AgCl}$. A large semicircle was observed in the Nyquist plot. The experimental data were fitted by an equivalent circuit as shown in the inset of Fig. 8, in which R_1 is an equivalent series resistance, R_2 is a resistance due to interfacial charge transfer and charge recombination, and CPE is a constant phase element associated with disorder in the electrode. The impedance of CPE is given by

$$Z_{CPE} = \frac{1}{(j\omega)^P T} \tag{2}$$

where j is an imaginary unit, ω is angular frequency, P is the exponential term, and T is the magnitude of admittance at ω=1 rad s^{-1}. When P is close to 1.0, the CPE resembles a capacitor, in which T is close to the capacitance. The parameters obtained by fitting are summarized in Table 1. The values of R_1 and P were almost constant, whereas R_2, i.e., the diameter of semicircle, was increased and T was

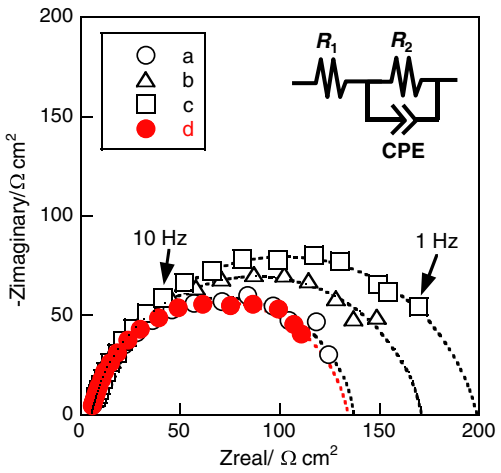

Fig. 8 Impedance spectra of W180-1 h-C during photoelectrochemical oxidation of water in 0.1 mol L^{-1} H_2SO_4 at +0.8 $V_{Ag/AgCl}$: (*a*) first run, (*b*) second run, (*c*) third run, and (*d*) fourth run after regeneration by cyclic voltammetry. The *symbols* and *dashed arcs* represent the experimental data and fitted curves, respectively

Table 1 Circuit parameters obtained by fitting the impedance results

Run	R_1 (Ω cm^2)[a]	R_2 (Ω cm^2)[b]	P[c]	T (μF s$^{(P-1)}$ cm^{-2})[c]
1st	5.40±2.7%	132±1.6%	0.93±0.7%	494±2.8%
2nd	5.39±2.2%	166±1.1%	0.89±0.4%	440±1.8%
3rd	5.86±2.6%	193±1.1%	0.88±0.5%	399±1.9%
4th	5.08±1.9%	129±1.2%	0.92±0.5%	580±2.0%

[a] Equivalent series resistance

[b] Resistance due to interfacial charge transfer and charge recombination

[c] $Z_{CPE} = \{(j\omega)^P T\}^{-1}$

decreased with a repetition of the run. The increase of R_2 indicates that the resistance of W180-1 h-C was elevated with the photoelectrochemical reaction. However, the EIS response was restored to the original response after cyclic voltammetry, indicating that the electrode was fully regenerated by the reduction and removal of the partially oxidized species at negative potential.

Although the platelet structures of W100-3 h-C, W140-2 h-C, and W180-1 h-C were similar, the photoelectrochemical properties for water splitting were quite different. Since the crystal transformation from the precursors to WO_3 was not perfect, and the surfaces of the WO_3 platelets were not smooth, we could not differentiate the crystal lattice planes primarily exposed on the WO_3 platelets. The presence of variances in the reaction selectivity suggests that there might be disparities between the surface nanostructures. Therefore, the selectivity for oxygen evolution or the production of partially oxidized intermediates may also vary. These results and considerations lead to the conclusion that catalytic oxygen evolution is significantly affected by the nanostructures on the WO_3 surface.

Finally, we performed an action spectrum analysis of W180-1 h-C for the photoelectrochemical oxidation of methanol (Fig. 9). The incident photon-to-current conversion efficiencies (IPCEs) were evaluated from photocurrent–time plots at +0.8 $V_{Ag/AgCl}$ under monochromatic photoirradiation. The onset wavelength of the action spectrum was close to the photoabsorption edge of reflectance (R) spectrum that is responsive to the violet portion of the visible light spectrum. Therefore, it functions with high efficiency under the conditions of visible light irradiation, without UV light. The IPCE under 365-nm photoirradiation was found to be more than 100%, suggesting the presence of the current doubling effect. The high efficiency is likely due to the large surface area and high crystallinity owing to the nanocrystalline platelet structures, although further studies are warranted to elucidate the kinetics behind this high efficiency.

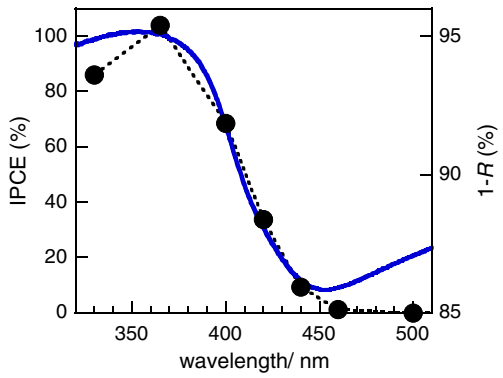

Fig. 9 Action spectrum of IPCEs for W180-1 h-C in 0.1 mol L^{-1} H_2SO_4 with 10 vol.% methanol at +0.8 $V_{Ag/AgCl}$. Diffuse reflectance UV–vis spectrum of W180-1 h-C is also shown

Conclusion

Monoclinic WO_3 thin film electrodes comprised of rectangular platelets exhibited a high efficiency for the photoelectrochemical oxidation of water and methanol. The stability and selectivity of the thin films prepared via $WO_3 \cdot H_2O$ platelets with the {010} facet were different from that of the thin films prepared via $WO_3 \cdot 2H_2O$ platelets with the {010} facet, although both platelets exhibited the same crystal lattice planes. The photocurrent of the WO_3 thin films prepared via $WO_3 \cdot H_2O$ platelets declined faster than that of the WO_3 thin films, which were prepared via $WO_3 \cdot 2H_2O$ platelets during water splitting, but it could be regenerated by treatments of cyclic voltammetry, suggesting that the decline is attributable to the formation and accumulation of partially oxidized products, such as peroxo species, on the surface. The partially oxidized species were reduced and removed at a negative potential in the cyclic voltammetry. Since the crystal transformations from the rectangular platelets of layered $WO_3 \cdot H_2O$ and $WO_3 \cdot 2H_2O$ to monoclinic WO_3 were not perfect, the surface structures of the WO_3 platelets were not uniform at the nanometer scale. These

results suggest that the efficacy in the catalytic oxygen evolution reaction was significantly affected by the nanostructures that were present on the surface, which cannot be distinguished via SEM observation.

Acknowledgements This work was supported by the Institutional Program for Young Researcher Overseas Visits from the Japan Society for the Promotion of Science (JSPS) and a Grant-in-Aid for Young Scientists (A) (No. 23686114) from JSPS.

References

1. Ma RZ, Sasaki T (2010) Adv Mater 22:5082–5104
2. Schaak RE, Mallouk TE (2002) Chem Commun:706–707
3. Takagaki A, Sugisawa M, Lu DL, Kondo JN, Hara M, Domen K, Hayashi S (2003) J Am Chem Soc 125:5479–5485
4. Ida S, Ogata C, Eguchi M, Youngblood WJ, Mallouk TE, Matsumoto Y (2008) J Am Chem Soc 130:7052–7059
5. Maeda K, Eguchi M, Lee SHA, Youngblood WJ, Hata H, Mallouk TE (2009) J Phys Chem C 113:7962–7969
6. Manga KK, Zhou Y, Yan YL, Loh KP (2009) Adv Funct Mater 19:3638–3643
7. Yu SH, Liu B, Mo MS, Huang JH, Liu XM, Qian YT (2003) Adv Funct Mater 13:639–647
8. Chen SH, Carroll DL (2002) Nano Lett 2:1003–1007
9. Sigman MB, Ghezelbash A, Hanrath T, Saunders AE, Lee F, Korgel BA (2003) J Am Chem Soc 125:16050–16057
10. Tian ZRR, Voigt JA, Liu J, McKenzie B, McDermott MJ, Rodriguez MA, Konishi H, Xu HF (2003) Nature Mater 2:821–826
11. Zhang YW, Sun X, Si R, You LP, Yan CH (2005) J Am Chem Soc 127:3260–3261
12. Liu JP, Li YY, Huang XT, Li GY, Li ZK (2008) Adv Funct Mater 18:1448–1458
13. Jun YW, Casula MF, Sim JH, Kim SY, Cheon J, Alivisatos AP (2003) J Am Chem Soc 125:15981–15985
14. Wei GZ, Lu X, Ke FS, Huang L, Li JT, Wang ZX, Zhou ZY, Sun SG (2010) Adv Mater 22:4364–4367
15. Lazzeri M, Vittadini A, Selloni A (2001) Phys Rev B: Condens Matter 63:155409
16. Chen DL, Gao L, Yasumori A, Kuroda K, Sugahara Y (2008) Small 4:1813–1822
17. Widenkvist E, Quinlan RA, Holloway BC, Grennberg H, Jansson U (2008) Cryst Growth Des 8:3750–3753
18. Amano F, Li D, Ohtani B (2010) Chem Commun 46:2769–2771
19. Amano F, Li D, Ohtani B (2011) J Electrochem Soc 158:K42–K46
20. Chen D, Ye JH (2008) Adv Funct Mater 18:1922–1928
21. Erbs W, Desilvestro J, Borgarello E, Grätzel M (1984) J Phys Chem 88:4001–4006
22. Ohno T, Tanigawa F, Fujihara K, Izumi S, Matsumura M (1998) J Photochem Photobiol A 118:41–44
23. Wang HL, Lindgren T, He JJ, Hagfeldt A, Lindquist SE (2000) J Phys Chem B 104:5686–5696
24. Santato C, Ulmann M, Augustynski J (2001) Adv Mater 13:511–514
25. Arai T, Horiguchi M, Yanagida M, Gunji T, Sugihara H, Sayama K (2008) Chem Commun:5565–5567
26. Abe R, Takami H, Murakami N, Ohtani B (2008) J Am Chem Soc 130:7780–7781
27. Miseki Y, Kusama H, Sugihara H, Sayama K (2010) J Phys Chem Lett 1:1196–1200
28. Macphee DE, Rosenberg D, Skellern MG, Wells RP, Duffy JA, Killham KS (2011) J Solid State Electrochem 15:99–103
29. Berger S, Tsuchiya H, Ghicov A, Schmuki P (2006) Appl Phys Lett 88:203119
30. Kalantar-zadeh K, Vijayaraghavan A, Ham MH, Zheng HD, Breedon M, Strano MS (2010) Chem Mater 22:5660–5666
31. Jiao ZH, Wang JM, Ke L, Sun XW, Demir HV (2011) ACS Appl Mater Interfaces 3:229–236
32. Su JZ, Feng XJ, Sloppy JD, Guo LJ, Grimes CA (2011) Nano Lett 11:203–208
33. Ng C, Ye CH, Ng YH, Amal R (2010) Cryst Growth Des 10:3794–3801
34. Shibuya M, Miyauchi M (2009) Adv Mater 21:1373–1376
35. Szymanski JT, Roberts AC (1984) Can Mineral 22:681–688
36. Li YM, Hibino M, Miyayania M, Kudo T (2000) Solid State Ionics 134:271–279
37. Yagi M, Maruyama S, Sone K, Nagai K, Norimatsu T (2008) J Solid State Chem 181:175–182
38. Amano F, Tian M, Wu G, Ohtani B, Chen A (2011) ACS Appl Mater Interfaces 3:4047–1052
39. Daniel MF, Desbat B, Lassegues JC, Gerand B, Figlarz M (1987) J Solid State Chem 67:235–247
40. Pecquenard B, Lecacheux H, Livage J, Julien C (1998) J Solid State Chem 135:159–168
41. Chemseddine A, Babonneau F, Livage J (1987) J Non-Crystalline Solids 91:271–278
42. Yamakata A, Ishibashi T, Onishi H (2001) J Phys Chem B 105:7258–7262
43. Yamakata A, Ishibashi T, Onishi H (2002) J Phys Chem B 106:9122–9125
44. Santato C, Ulmann M, Augustynski J (2001) J Phys Chem B 105:936–940
45. Peter LM (1990) Chem Rev 90:753–769
46. Augustynski J, Solarska R, Hagemann H, Santato C (2006) Proc SPIE 6340:63400J
47. Seabold JA, Choi KS (2011) Chem Mater 23:1105–1112